Received: 19 May 2024 | Revised: 1 September 2024 | Accepted: 17 September 2024

DOI: 10.1002/nbm.5266

RESEARCH ARTICLE

NMR IN BIOMEDICINE WILEY

Accelerated 2D radial Look-Locker T1 mapping using a deep learning-based rapid inversion recovery sampling technique

Eze Ahanonu[1] | Ute Goerke[2] | Kevin Johnson[3] | Brian Toner[4] | Diego R. Martin[5] | Vibhas Deshpande[6] | Ali Bilgin[1,3,4,7] | Maria Altbach[3,7]

[1]Department of Electrical and Computer Engineering, The University of Arizona, Tucson, Arizona, USA

[2]Siemens Medical Solutions USA, Tucson, Arizona, USA

[3]Department of Medical Imaging, The University of Arizona, Tucson, Arizona, USA

[4]Applied Math Program, The University of Arizona, Tucson, Arizona, USA

[5]Department of Radiology, Houston Methodist Hospital, Houston, Texas, USA

[6]Siemens Medical Solutions USA, Austin, Texas, USA

[7]Department of Biomedical Engineering, The University of Arizona, Tucson, Arizona, USA

Correspondence
Maria Altbach, Department of Medical Imaging, The University of Arizona, 1501 N. Campbell Ave., P.O. Box 245067, Tucson, Arizona 85724, USA.
Email: maltbach@arizona.edu

Funding information
Arizona Biomedical Research Centre, Grant/Award Number: CTR056039; National Institutes of Health, Grant/Award Numbers: CA245920, EB031894, HL4038940, AG070987; Technology and Research Initiative Fund (TRIF) Improving Health Initiative

Abstract

Efficient abdominal coverage with T1-mapping methods currently available in the clinic is limited by the breath hold period (BHP) and the time needed for T1 recovery. This work develops a T1-mapping framework for efficient abdominal coverage based on rapid T1 recovery curve (T1RC) sampling, slice-selective inversion, optimized slice interleaving, and a convolutional neural network (CNN)-based T1 estimation. The effect of reducing the T1RC sampling was evaluated by comparing T1 estimates from T1RC ranging from 0.63 to 2.0 s with reference T1 values obtained from T1RC = 2.5–5 s. Slice interleaving methodologies were evaluated by comparing the T1 variation in abdominal organs across slices. The repeatability of the proposed framework was demonstrated by performing acquisition on test subjects across imaging sessions. Analysis of in vivo data based on retrospectively shortening the T1RC showed that with the CNN framework, a T1RC = 0.84 s yielded T1 estimates without significant changes in mean T1 ($p > 0.05$) or significant increase in T1 variability ($p > 0.48$) compared to the reference. Prospectively acquired data using T1RC = 0.84 s, an optimized slice interleaving scheme, and the CNN framework enabled 21 slices in a 20 s BHP. Analyses across abdominal organs produced T1 values within 2% of the reference. Repeatability experiments yielded Pearson's correlation, repeatability coefficient, and coefficient of variation of 0.99, 2.5%, and 0.12%, respectively. The proposed T1 mapping framework provides full abdominal coverage within a single BHP.

KEYWORDS
abdominal imaging, deep learning, Look-Locker, radial sampling, single-shot inversion recovery, T1 mapping

Abbreviations: ADAM, adaptive moment estimation; BART, Berkeley advanced reconstruction toolbox; BHP, breath hold period; CAD, cross-talk acquisition delay; CNN, convolutional neural network; CV, coefficient of variation; DL, deep learning; FLASH, fast low angle shot magnetic resonance imaging; GRAPPA, generalized autocalibrating partial parallel acquisition; GRE, gradient echo; LLR, locally low-rank regularization; MOLLI, modified Look-Locker inversion recovery; MSE, mean squared error; nsIR, non-slice-selective inversion recovery; NUFFT, non-uniform fast Fourier transform; OSI, optimized slice interleaving; PC, principal component; PWF, pixel-wise fitting; rLL, radial Look-Locker; RMSE, root mean square error; ROI, region of interest; RPC, repeatability coefficient; SE-IR, spin-echo inversion recovery; ShMOLLI, shortened modified Look-Locker inversion recovery; SNR, signal-to-noise ratio; SSFP, steady-state free-precession; SSI, standard slice interleaving; ssIR, slice-selective inversion recovery; SVD, singular value decomposition; T1RC, T1 recovery curve; TI, inversion time; TR, repetition time; VFA, variable flip angle.

1 | INTRODUCTION

T1 mapping enables quantitative evaluation of tissue for patient assessment and diagnosis of disease. In the abdomen, T1 mapping has demonstrated utility in detection and characterization of focal liver lesions[1,2] as well as the evaluation of chronic liver disease,[3] including liver fibrosis[4,5] and cirrhosis.[6,7] T1 mapping was also used to assess chronic pancreatitis[8] and the status of the kidney after transplantation.[9]

Currently, T1 mapping techniques available in the clinic are mainly based on Look-Locker techniques such as the modified Look-Locker inversion recovery (MOLLI)[10] and its shorter version shortened modified Look-Locker inversion recovery (ShMOLLI).[11] Both provide B1 insensitivity but are limited by inefficient anatomical coverage allowing the acquisition of only 1–2 slices within a single 20 s breath hold period (BHP). Techniques based on variable flip angle (VFA)[12] are also used clinically. They provide better coverage per unit time but are not preferred due to their B1 sensitivity.[13]

Techniques for multi-parameter estimation such as magnetic resonance fingerprinting[14] have been proposed[15,16] but do not yield improvements in anatomical coverage per unit time compared to MOLLI or ShMOLLI; these techniques are also sensitive to B0/B1 inhomogeneities.[17,18] Several techniques have been proposed for abdominal T1 mapping with the goal of providing more efficient coverage of the abdomen. Chen et al.[19] proposed an accelerated technique utilizing a stack-of-spirals trajectory combined with generalized autocalibrating partial parallel acquisition (GRAPPA)[20] to achieve abdominal T1 mapping of 32 slices within a 20 s BHP. The technique yields data for eight inversion time (TI) points acquired through multiple shots spread throughout the BHP, making it prone to errors in the T1 relaxation curve if there is motion during the breath hold. Feng et al.[21] proposed a stack-of-radials T1 mapping technique where data for the relaxation curve are acquired during free breathing. Their technique offers good anatomical coverage, but free breathing methods are also more prone to errors in T1 estimation due to motion.

Single-shot breath hold techniques based on a 2D radial Look-Locker (rLL) approach have also been proposed. These offer reduced motion sensitivity due to the radial k-space trajectory and the fact that all the TI data points used for T1 estimation are acquired within 3–4 s. Wang et al.[22] proposed a single-shot non-slice-selective inversion recovery (nsIR) radial fast low angle shot magnetic resonance imaging (FLASH) sequence, paired with simultaneous multi-slice acquisition, to acquire three slices within 4 s. Re-application of the nsIR must occur after a delay time (~4 s) to avoid the effects of T1 saturation, limiting the coverage of this technique to 9–10 slices within a BHP. Li et al.[23] proposed a single-shot slice-selective inversion recovery (ssIR) radial steady-state free-precession (SSFP) pulse sequence that enables acquisition of 10 slices within a BHP, without the need for a recovery time between inversions. Further slice efficiency within the ssIR approach is limited by the time required to sample the T1 recovery curve (T1RC) for accurate T1 estimation. Recently, there has been increased interest in fat-water-separated T1 mapping, and dual-echo single-shot Look-Locker-based techniques have been proposed for abdominal applications.[24,25] These techniques have demonstrated accurate T1 mapping of the tissue water component but are still limited in anatomical coverage due to required T1RC sampling time.

This work proposes a rapid ssIR rLL T1 mapping framework to enable full abdominal coverage in a single BHP through use of rapid T1RC sampling (<1 s), optimized slice interleaving (OSI), and deep learning (DL)-based T1 estimation. Experimental results demonstrate that this technique can double the slice efficiency of previously proposed breath hold rLL approaches,[22,23] allowing a proportional increase in anatomical coverage. Additionally, the reduced per-slice acquisition time further reduces motion sensitivity. The technique is demonstrated here in phantoms and in vivo abdominal imaging.

2 | METHODS

2.1 | Baseline abdominal T1 mapping technique

Figure 1A outlines the baseline ssIR rLL T1 mapping sequence used here as a reference. The sequence is a 2D radial method, which uses a 180° adiabatic hyperbolic secant ssIR RF pulse, followed by a train of gradient echo (GRE) readouts to acquire k-space radial views for a given slice. Data for each radial view are acquired after the ramp-up period, with a tiny golden angle increment (23.63°) between consecutive radial views. For improved inversion uniformity, the slice thickness of the inversion recovery (IR)-pulse is designed to be 200% of the nominal α-pulse slice thickness (see Figure S2). The acquired radial views for each slice are divided into undersampled TI groups ($\mathbf{K}_1$,...,$\mathbf{K}_N$) and used in a joint compressed-sensing iterative reconstruction to obtain a corresponding set of TI images ($\mathbf{I}_1$,...,$\mathbf{I}_N$). T1 maps are generated by pixel-wise fitting (PWF) of the signal evolution across TI images to a T1 signal model. The length of the GRE readout is made sufficiently long (≥2.5 s) to ensure adequate sampling of the T1RC for T1 estimation.

2.2 | Proposed rapid abdominal T1 mapping technique

Figure 1B outlines the proposed accelerated technique, which uses the same data acquisition as described in Section 2.1, but with a rapid GRE readout (<1 s) to reduce the time spent sampling the T1RC for each slice. For multi-slice acquisition, an OSI scheme is used to reduce T1

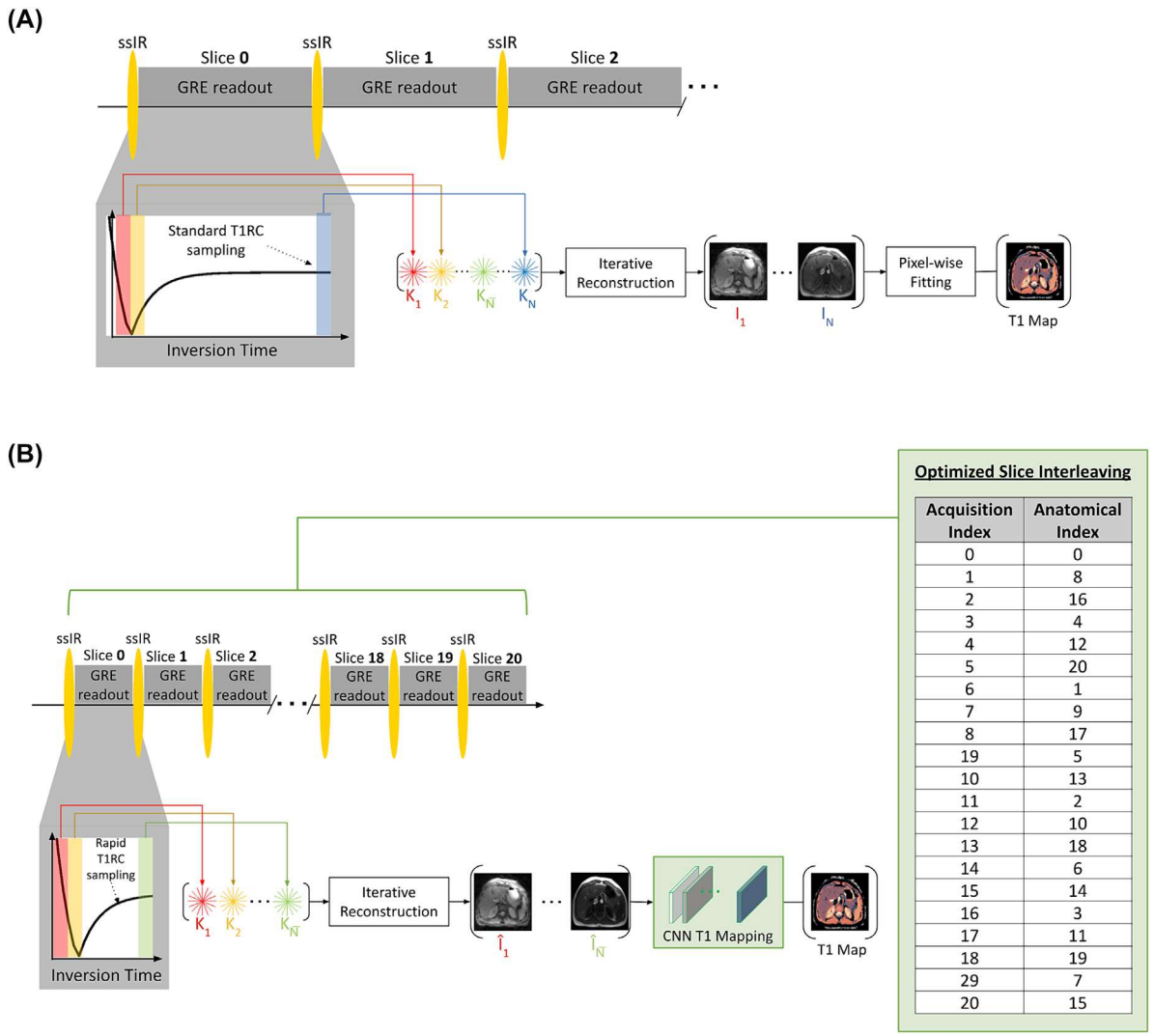

FIGURE 1 Diagrams of breath-hold slice-selective inversion recovery (ssIR) 2D radial look-locker (rLL) T1 mapping. (A) Baseline T1 mapping framework utilizing standard T1 recovery curve (T1RC) sampling and pixel-wise fitting, with slice anatomical acquisition order dependent on the prescribed protocol. (B) Proposed highly accelerated T1 mapping framework utilizing rapid T1RC sampling, convolutional neural network (CNN)-based T1 estimation, and optimized slice interleaving (OSI). For demonstration, the full OSI slice anatomical ordering for a 21-slice acquisition for $N_G = 4$ is provided (see Figure S3 for detailed construction).

saturation effects due to slice cross-talk (see Section 2.3). The reduced set of acquired radial views for each slice are divided into TI groups ($\mathbf{K} = \{\mathbf{K}_1,\ldots,\mathbf{K}_{\bar{N}}\}$; $\bar{N} < N$) and used in a joint compressed-sensing iterative reconstruction to obtain the corresponding reduced set of TI images ($\hat{\mathbf{I}} = \{\hat{\mathbf{I}}_1,\ldots, \hat{\mathbf{I}}_{\bar{N}}\}$). These TI images ($\hat{\mathbf{I}}$) will have reduced signal-to-noise ratio (SNR) due to fewer radial views being available for joint reconstruction. To maintain accurate T1 estimation, a DL model, which exploits spatio-temporal dependencies (see Section 2.6), is used to estimate T1 maps given reduced SNR TI images.

2.3 | Optimized slice interleaving (OSI)

Slice cross-talk due to the ssIR pulse will result in partial excitation of tissue within $+/-2$ nominal slice positions of the applied ssIR (see Figure S2). When employing rapid T1RC sampling, there will be insufficient spin-relaxation time within this tissue region to prevent T1 saturation, resulting in T1 underestimation. To minimize T1 saturation effects, slice interleaving may be used to increase the cross-talk acquisition delay (CAD), defined here as the time between application of an ssIR and acquisition of slices impacted by its cross talk. Standard slice interleaving (SSI) schemes, in which even followed by odd (or vice versa) indexed slice is acquired, do not provide adequate CAD to prevent T1 saturation due to subsequence acquisition of the $+/-2$ nominal slice position. To address this, we consider OSI schemes, which better distribute the ssIR's across

anatomy over time.[26] One such scheme[23] begins by partitioning the N_S prescribed anatomically ordered slices ($S_{ANA} = \{s_j \mid j = [0,1,...,N_S\text{-}1]\}$) into user defined N_G slice group sets ($\{SG_1,...,SG_{N_G}\}$) according to $SG_i = \{s_j \mid j = [0,1,...,N_S\text{-}1], (j \bmod N_G) = i\}$. Each SG_i is an ordered set of slices sorted by increasing index (j). The final slice order is constructed by performing SSI within each slice group ($\bar{SG}_i = SSI(SG_i)$). The optimal choice of N_G is determined by constructing OSI schemes with $N_G = [1,...,N_S]$ and choosing the N_G that maximizes the CAD.

2.4 | Data reconstruction and T1 estimation

TI images were reconstructed from the undersampled TI groups by using a principal component (PC) subspace constrained iterative reconstruction to exploit temporal dependencies, along with locally low-rank (LLR) regularization[27] to exploit sparsity in the PC domain. The reconstruction may be formulated by first considering the measured k-space data $\mathbf{K} \in \mathbb{C}^{N_t N_v N_r N_c \times 1}$, where N_t represents the number of TI groups, N_v the number of radial views per TI group, N_r the GRE readout length, and N_c the number of coils. We then define the operator $F(.)$ to be the non-uniform Fourier transform with embedded coil sensitivity encoding so that $\mathbf{K} = F(\mathbf{I})$ relates $\mathbf{K}$ to the TI images $\mathbf{I} \in \mathbb{C}^{N_t \times N_s}$, with N_s representing the number of spatial pixels.

The PC basis is computed by using the Bloch equations to simulate T1 IR over the N_t TI points ($\overrightarrow{TI} = [TI_1,...,TI_{N_t}]$) for a chosen set of T1 and B1 values. The signal vector for a single T1 and B1 value pair ($T1_i$ and $B1_j$) may be represented by $\overrightarrow{\mathbf{s}_{ij}} = S(\overrightarrow{TI}, T1_i, B1_j, B0, TE, TR, \alpha)$, where the function $S(.)$ generates the signal vector across the N_t TI points. The set of signal vectors $\{\overrightarrow{\mathbf{s}_{ij}}\}$ for all T1 and B1 value pairs are then used in a singular value decomposition (SVD) analysis to obtain the basis $\mathbf{B} \in \mathbb{C}^{N_t \times N_t}$, whose columns contain the estimated PCs sorted from most to least significant. The PC subspace $\bar{\mathbf{B}} \in \mathbb{C}^{N_t \times N_{pc}}$ is generated by taking the first N_{pc} columns of $\mathbf{B}$. Given the PC coefficient matrix $\mathbf{P} \in \mathbb{C}^{N_{pc} \times N_s}$, the TI images ($\mathbf{I}$) may be estimated as $\mathbf{I} \approx \bar{\mathbf{B}}\,\mathbf{P}$. The iterative reconstruction problem may then be formulated as

$$\hat{\mathbf{P}} = \arg\min_{\mathbf{P}} \|\mathbf{K} - F(-\mathbf{B}\mathbf{P})\|_2^2 + \lambda_S \sum_{\boldsymbol{\omega} \in \Omega_{\lambda_B}(\mathbf{P})} \|\boldsymbol{\omega}\| \tag{1}$$

where $\Omega_{\lambda_B}(.)$ represents an operator, which randomly partitions $\mathbf{P}$ into a set of non-overlapping spatial-blocks $\boldsymbol{\omega} \in \mathbb{C}^{\lambda_B \lambda_B \times 1}$. The operation $\|.\|_*$ represents the nuclear norm, and λ_S gives the LLR regularization weight. Equation (1) is minimized iteratively, with the partition $\Omega_{\lambda_B}(.)$ updated after each iteration to minimize LLR blocking artifacts.[28] The final reconstructed TI images are generated as $\hat{\mathbf{I}} = -\mathbf{B}\hat{\mathbf{P}}$.

For all experiments, Bloch simulation for PC basis construction was performed for T1 values ranging from 100 to 3000 ms in increments of 1 ms, and B1 values ranging from 0.2 to 2.4 in increments of 0.2. Parameters used for reconstruction were $N_{pc} = 4$, $\lambda_B = 8$, and $\lambda_S = 1.0e{-}14$ (in vivo) or $1.0e{-}18$ (phantoms). For PWF, T1 maps were generated by dictionary fitting the reconstructed signal evolutions across TI images to the same library used in PC basis construction.

The above iterative reconstruction and T1 fitting routines were implemented in MATLAB (MathWorks, MA, USA). Sensitivity maps were estimated utilizing the Berkeley Advanced Reconstruction Toolbox (BART) *ecalib* tool[29] with a kernel size of 4 and calibration region size of 16. Non-uniform fast Fourier transform (NUFFT) operations were performed using the open source gpuNUFFT library.[30] The per-slice reconstruction time was ~5 min on a workstation with an Intel Xeon E5-2630 v4 CPU, 128GB RAM, and a NVIDIA TITAN X GPU.

2.5 | MRI experiments

The 2D ssIR rLL pulse sequence was implemented at 3 T (MAGNETOM Skyra, Siemens Healthcare, Erlangen, Germany). Phantom experiments were performed using a 32-channel head receiver coil. In vivo experiments were performed using an 18-channel body surface array and 32-channel spine coil. Subject-specific coil selection was performed to cover the liver and kidneys.

Phantom experiments were performed to assess the impact of the accelerated T1RC on T1 estimation. Phantoms consisted of 50 mL vials with 2% agarose (for adjusting T2 ~40 ms) $NiCl_2$ solutions (0.28, 0.74, 1.19, and 2.1 mM) to produce a range of T1 values as those found in the abdomen. Acquisition was performed with slice thickness = 8 mm, repetition time (TR) = 3.3 ms, echo time (TE) = 1.3 ms, $\alpha = 10^{\circ}$, base resolution = 256, field of view (FOV) = 400 mm, and initial TI (defined as the time between the midpoints of the ssIR and the first alpha RF pulse) of 15.3 ms. The acquisition consisted of 992 radial views to produce a reference T1RC of 5 s. Reconstruction and T1 estimation were performed using the method described in Section 2.4. Reference T1 values for each vial were obtained from a spin-echo inversion recovery (SE-IR) acquisition at TI = [50, 150, 300, 500, 750, 1000, 1500, 2000, 3000, 4000 ms]. Scanner-generated magnitude SE-IR images were then used to estimate T1 maps by fitting each pixel across TI images to the T1 IR signal model.[31]

This study was approved by the Institutional Review Board. Imaging experiments were performed on a cohort of 30 subjects (18 males, 12 females, 23–73 years old) after obtaining informed consent. For development, this cohort was randomly split into 20 training subjects (12 males, 8 females, 31–73 years old) and 10 testing subjects (six males, four females, 23–62 years old). For all subjects, abdominal axial slices

were acquired with slice thickness = 8 mm, TR = 3.3 ms, TE = 1.75 ms, $\alpha = 10^{\circ}$, base resolution = 256, FOV = 400 mm, and initial TI = 15.3 ms. For each subject, data were acquired using the baseline protocol with 768 radial views to produce a T1RC of 2.5 s. Acquisition consisted of a 21-slice volume divided over three 20 s BHPs with seven slices per BHP spread over the 21-slice volume; this ensured at least a 200% slice gap between subsequent acquisitions.

For test subjects, additional abdominal data were acquired using the accelerated T1 mapping pulse sequence. Data were acquired with the same parameters as the in vivo baseline sequence except that only 256 radial views were acquired to achieve a rapid 0.84 s T1RC sampling. This allowed for the acquisition of 21 slices in a single 20 s BHP. Choice of OSI grouping parameter N_G for $N_S = 21$ was made by assessing CAD across slices for $N_G = [1, 2, ..., 21]$. From this, it was determined that $N_G = 4$ was optimal, providing a CAD ≥ 4200 ms across all slices. This CAD would provide sufficient spin-relaxation time to minimize the effects of T1 saturation. This resulted in a final OSI slice order of [0, 8, 16, 4, 12, 20, 1, 9, 17, 5, 13, 2, 10, 18, 6, 14, 3, 11, 19, 7, 15] (see Figure S3). For comparison, data were also acquired using the SSI scheme to produce the anatomical acquisition order: [0, 2, 4, 6, 8, 10, 12, 14, 16, 18, 20, 1, 3, 5, 7, 9, 11, 13, 15, 17, 19]. For assessment of repeatability, the 0.84 s T1RC protocol was repeated on the same subjects in the same scanning session with the subject stepping out of and back into the scanner between scans.

2.6 | Convolutional neural network (CNN) training and testing framework

To enable accurate T1 estimation from reduced T1RC data, a fully supervised framework was implemented to train a CNN to estimate T1 maps given highly undersampled TI images. The proposed training framework is summarized in Figure 2 for a single slice. Data acquired on the training subject cohort using the baseline ssIR rLL technique underwent iterative reconstruction to obtain TI images ($\mathbf{I}_1,...,\mathbf{I}_N$) and T1 maps corresponding to standard-T1RC sampling ($T1_{ref}$). K-space data were then retrospectively truncated to produce a dataset ($\mathbf{K}_1,...,\mathbf{K}_{\bar{N}}$, $\bar{N} < N$) to simulate acquired accelerated T1RC data due to a shortened GRE readout. This dataset was reconstructed iteratively (see Section 2.3) to obtain a corresponding truncated set of TI images ($\hat{\mathbf{I}}_1,...,\hat{\mathbf{I}}_{\bar{N}}$). Because the radial views from the TIs $i > \bar{N}$ are not available during joint iterative reconstruction, the TI images $\hat{\mathbf{I}}_i$ will have reduced SNR.

During training, the truncated set of TI images ($\hat{\mathbf{I}}_1,...,\hat{\mathbf{I}}_{\bar{N}}$) are given as network input, and the corresponding $T1_{ref}$ as label. The fitted CNN model produces an estimate ($T1_{est}$) of the T1 map that would be obtained from a standard T1RC acquisition. For testing and model deployment, the accelerated acquisition and reconstruction protocol outlined in Figure 1B are used to directly obtain a reduced TI image set. The pre-trained CNN model is then used to estimate the corresponding T1 maps. All CNN models were implemented in Python using the TensorFlow DL framework.[32] A ResNet[33] CNN architecture was used, which consists of 20 residual blocks, with each block containing two 32-filter convolutional layers. Training is performed for 3000 epochs using a mean square error (MSE) loss with a batch size of 64 using adaptive moment estimation (ADAM) optimization[34] with $\beta_1 = 0.9$, $\beta_2 = 0.999$, $\epsilon = 1.0e{-}8$, and a fixed learning rate of 1.0e−4. Training was performed on corresponding 32 × 32 pixel patches extracted from corresponding spatial regions within TI images (with dimensions 32 × 32 × $\bar{N}$) and T1 maps (with dimensions 32 × 32). For data augmentation, random spatial transformations (flip/rotation) were performed during training. CNN models were implemented for $\bar{N} = 12$, 16, 19, and 28 to produce corresponding T1RCs of 0.63, 0.84, 1.0, and 1.5 s, respectively, when using a TR of 3.3 ms with 16 views/TI group.

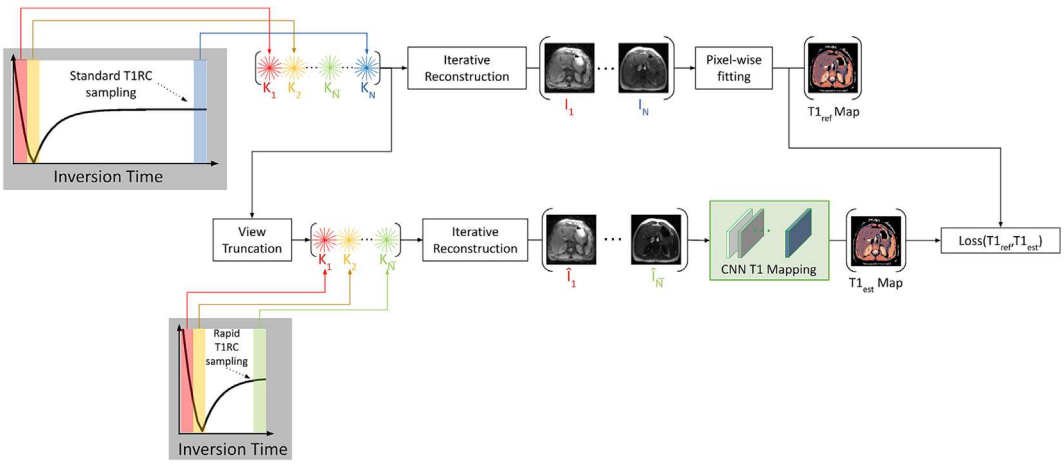

FIGURE 2 Convolutional neural network (CNN) training framework. K-space radial views acquired with a standard T1 recovery curve (T1RC) sampling are split into N undersampled TI groups ($\mathbf{K}_1,...,\mathbf{K}_N$) and used in an iterative reconstruction to obtain corresponding TI images ($\mathbf{I}_1,...,\mathbf{I}_N$) which are used with pixel-wise fitting to obtain the reference T1 map ($T1_{ref}$). Radial views are then truncated to produce a simulated rapid T1RC dataset ($\mathbf{K}_1,...,\mathbf{K}_{\bar{N}}$), which is used in iterative reconstruction to obtain a truncated image set ($\hat{\mathbf{I}}_1,...,\hat{\mathbf{I}}_{\bar{N}}$). A CNN is then trained to produce T1 map estimates ($T1_{est}$) given the truncated image set.

2.7 | Data and statistical analysis

For the retrospective data, region-of-interest (ROI) analysis was performed for the evaluation of T1 estimation across T1RC lengths for PWF and CNN-generated values. For phantom data, a 7 × 7 pixel ROI was chosen at the center of each vial. For in vivo data, for each slice where tissue was present, a 5 × 5 pixel ROI was selected from liver, muscle, spleen, and/or kidney cortex. For phantom and in vivo data, identical ROIs were used across T1RC lengths to allow pixel-wise comparison of T1 values. Within each ROI, the pixel-wise estimation error was computed as the mean and standard deviation of the relative absolute estimation error expressed as a percentage. Statistical significance of T1 means were compared using a *t*-test (significance level = 0.05), with $p > 0.05$ indicating insufficient evidence to reject the null hypothesis of equal means in favor of the alternative hypothesis of unequal means. For T1 variability, a right-sided *F*-test (significance level = 0.05) was used with a null hypothesis of equal variances, and an alternative hypothesis that T1 variability for the test method is greater than the reference method. Here, $p > 0.05$ indicated that insufficient evidence exists to reject the null hypothesis of equal variances, in favor of the alternative that the test method results in higher T1 variability.

In prospective analysis, data for different T1RC lengths were acquired within separate BHPs. Here, misalignment/misregistration of slices between acquisitions prevented the use of pixel-wise analysis. Thus, for data acquired prospectively within each protocol, ROIs were collected from each slice for each tissue (if present). The resulting values were then pooled, and the T1 mean and standard deviation were computed. Slice interleaving methods were compared by selecting ROIs from liver, muscle, spleen, and kidney cortex for each test subject from baseline, accelerated with SSI, and accelerated with OSI acquisitions. Concordance between baseline and accelerated techniques was assessed using linear regression analysis, with the best-fit equation and goodness of fit (R^2) used for assessment. Additionally, histogram analysis (with bin size of 50 ms) was performed to assess central tendency and variability for T1 values generated using PWF and CNN in accelerated acquisition.

To assess repeatability of the proposed accelerated protocol, linear regression and Bland–Altman analysis was performed to compare the mean T1 value estimates across organs. Here, the mean T1 value of each organ was computed over the pooled population of pixels stemming from ROIs across slices.

3 | RESULTS

3.1 | Retrospective assessment of T1RC length

3.1.1 | Phantom experiments

The impact of T1RC length on T1 estimation using PWF was assessed in a phantom containing four vials with varying T1 values representative of those encountered in the abdomen. Reference T1 values of vials 1, 2, 3, and 4 obtained using the baseline rLL protocol with T1RC = 5.0 s were 514, 782, 1027, and 1692 ms, respectively. SE-IR acquisition over the same respective vials yielded similar values of 531, 812, 1072, and 1778 ms. Figure 3A shows computed T1 maps using PWF at each T1RC length. Figure 3B gives computed root mean square error (RMSE) values within each vial across T1RC, with T1RC = 5.0 s as reference. Figure 3C shows box plots for estimated T1 values within each vial ROI across T1RC length.

As seen in Figure 3, the T1 maps for T1RC = 2.5–5.0 s show little to no appreciable difference (Figure 3A) with no statistically significant difference in T1 mean or standard deviation detected across vials (Figure 3B). Within this T1RC range, the pixel-wise T1 error also remains low at <1% across vials (Figure 3C). For T1RC = 2.0 s, a modest increase in noise may be observed for the longest T1 vial (vial 4), and a statistically significant increase in T1 variability was detected at this point. Further reduction of T1RC sampling results in increasing noise within T1 maps, with the longer T1 vials showing a stronger effect. Concomitantly, both significant increases in T1 standard deviation and significant differences in T1 mean are detected across multiple vials. The pixel-wise error across vials shows a similar effect, with the magnitude increasing with vial T1 value.

3.1.2 | In vivo experiments

Based on the phantom results (i.e., no significant changes in mean and standard deviation), it was determined that a T1RC = 2.5 s was suitable to achieve accurate T1 estimation with PWF. Thus, the baseline rLL T1 mapping in vivo protocol was implemented with a 2.5 s T1RC. The resulting dataset underwent retrospective view truncation to produce datasets with T1RC lengths as described in Section 2.6. These datasets were used to train a series of CNNs for varying T1RC lengths, with 20 subjects used in training and 10 subjects retained for testing. Evaluation was performed by comparing T1 estimation for each T1RC length between PWF and the proposed CNN approach on the test set. Figure 4 provides quantitative results comparing T1 values between PWF and CNN across T1RC lengths for ROIs in liver (L), muscle (M), spleen (S), and kidney cortex (K). Figure 4A shows box plots for the estimated T1 values within a given tissue ROI, while Figure 4B shows box plots for the pixel-wise T1 estimation error. Figure 5 shows qualitative results when applying PWF and CNN to the same anatomical slice for various T1RC lengths.

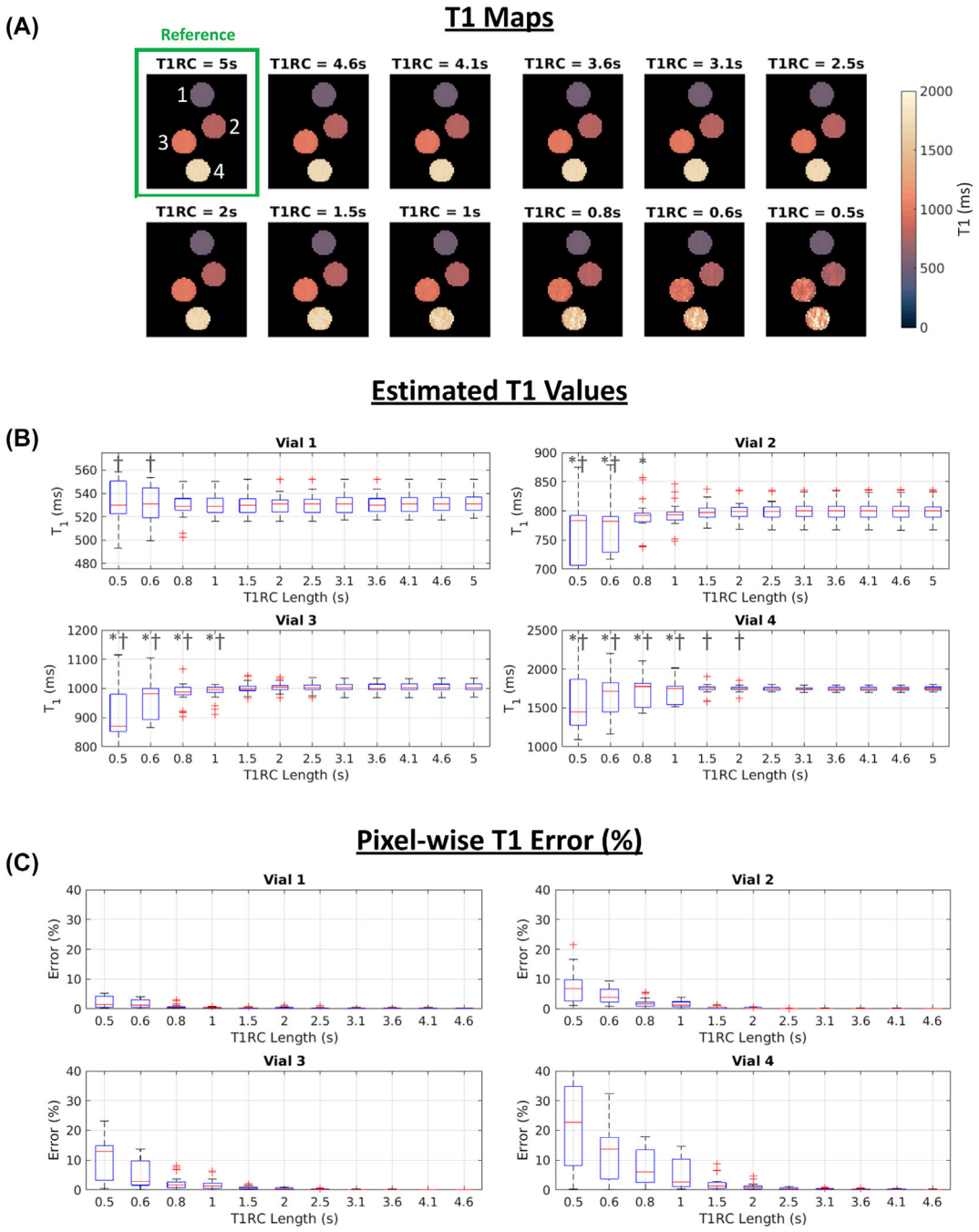

FIGURE 3 Impact of T1 recovery curve (T1RC) sampling in a phantom. (A) Computed T1 maps across T1RC sampling periods. (B) Box plots showing estimated T1 values for each phantom vial. Within each plot, * and † denote significance for mean and standard deviation, respectively. (C) Box plots showing relative pixel-wise T1 error within each phantom vial, with the 5 s T1RC dataset as reference.

For a T1RC = 1.5 s, we did not observe a statistically significant difference in T1 mean or standard deviation for PWF and CNN generated values and pixel-wise error remained low for both methods (PWF < 2.5%, CNN < 3%). For T1RC = 0.84–1.0 s, a statistically significant increase in T1 variability for PWF is detected, while no difference is observed statistically for CNN. Visualization of T1 maps shows a noticeable increase in noise for the PWF maps that is not observed in the CNN computed maps. For the shortest tested T1RC = 0.63 s, a statistically significant increase is detected for muscle, spleen, and kidney for PWF generated values; for CNN-generated values, a statistically significant increase in T1 variability was detected in kidney. At this T1RC length, we additionally observed significant changes in T1 mean for kidney in PWF, and for muscle in CNN. Qualitative observation of T1 maps shows PWF maps with appreciable levels of noise, in particular in long T1 tissue regions (e.g., kidney, spleen), while the CNN-generated maps are largely free of noise or other distortions.

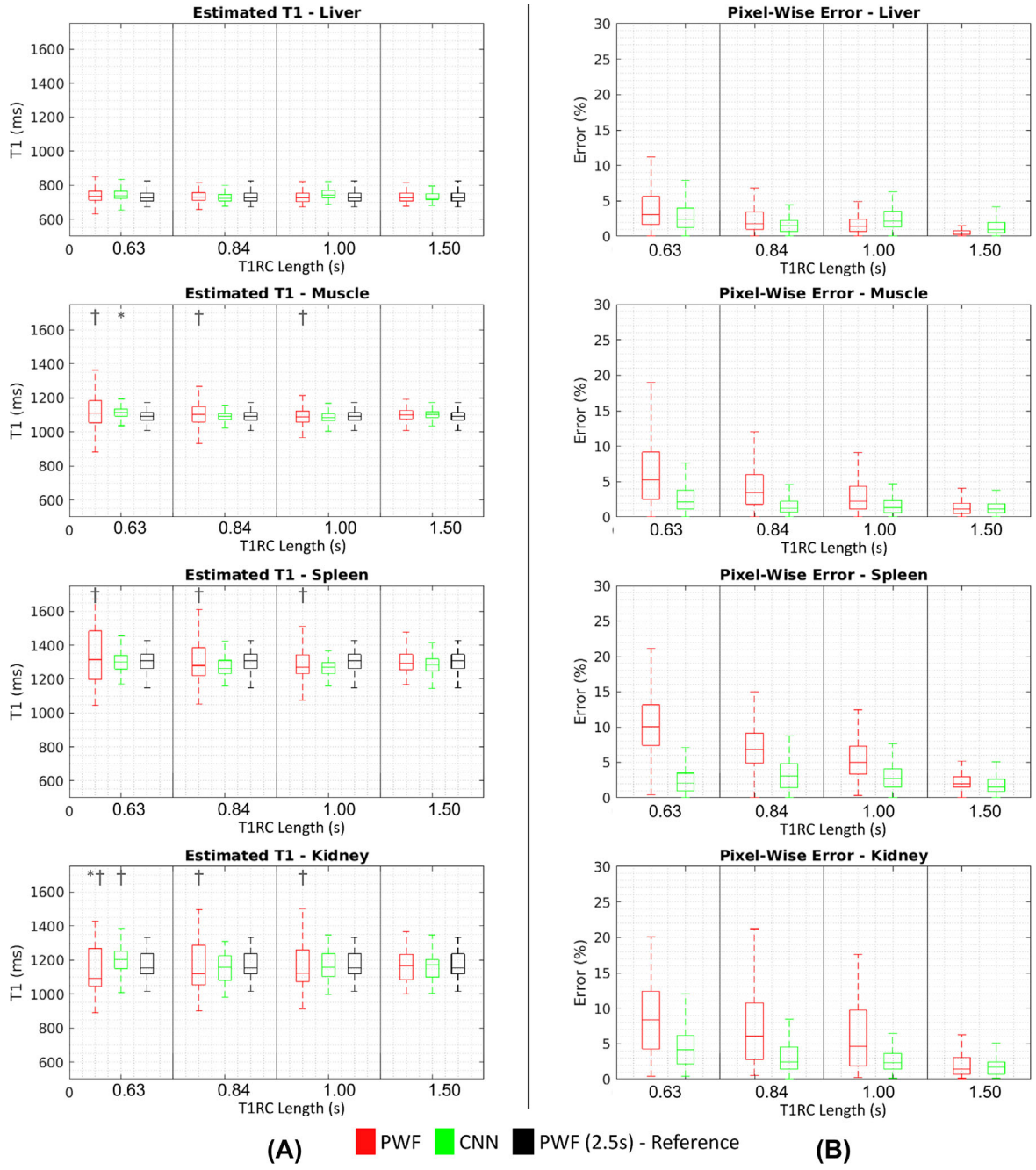

FIGURE 4 Impact of T1 recovery curve (T1RC) length on T1 estimation using in vivo data. T1RC are generated retrospectively by truncating radial views from data acquired with T1RC = 2.5 s. (A) Box plots for the estimated T1 values within liver, muscle, spleen, and kidney regions of interest. Within each plot, * and † denote significance for mean and standard deviation, respectively. (B) Box plots for the pixel-wise T1 estimation error within the same tissue regions. The red boxes correspond to the pixel-wise fitting (PWF) data, and the green boxes correspond to the proposed convolutional neural network (CNN) approach. The reference values, computed using PWF with a 2.5 s T1RC, are given in black.

3.2 | Prospective in vivo results

The results presented in Section 3.1 were used to develop the prospective accelerated protocol described in Section 2.5, which utilizes a T1RC of 0.84 s to acquire 21 slices using OSI within a single 20 s BHP, using the proposed CNN approach for T1 estimation.

The use of retrospective view truncation allowed efficient generation of training datasets over a range of input T1RC sampling lengths. To verify no domain shift will occur, we compared prospectively acquired and retrospectively generated datasets (see Figure S4). Qualitative evaluation of TI images across these datasets did not show any appreciable difference between the two datasets. Similarly, assessment of T1 IR signal evolution across liver, kidney (cortex), and spleen regions-of-interest also showed no appreciable difference between prospective and

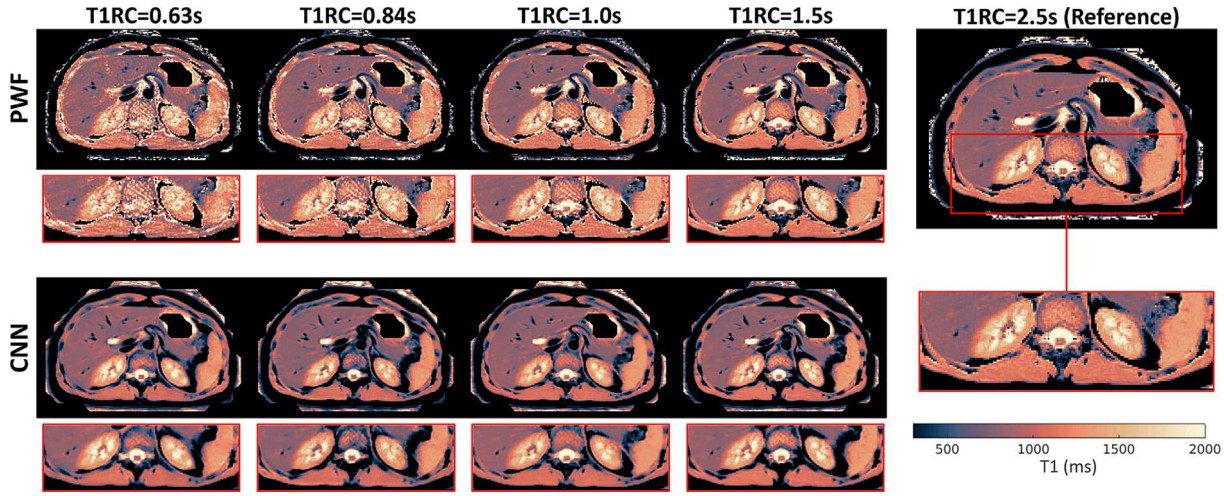

FIGURE 5 Abdominal T1 maps generated with retrospectively truncated T1 recovery curve (T1RC) using pixel-wise fitting (PWF) and the proposed convolutional neural network (CNN) approach for a test subject. Data show retention of T1 mapping quality for CNN even within long T1 regions (e.g., kidney, muscle, and spleen) for T1RC down to 0.63 s.

retrospective datasets. These observations indicate that no apparent domain shift is present that may impact the CNN T1 estimates when applied to prospectively acquired data.

3.2.1 | Effect of slice interleaving scheme

Figure 6 compares a baseline (T1RC = 2.5 s) 21-slice *multi*-BHP acquisition (Figure 6A) to an accelerated (T1RC = 0.84 s) 21-slice *single*-BHP acquisition using both SSI (Figure 6B) and OSI (Figure 6C) on the same subject. When compared to the baseline acquisition, SSI demonstrates T1 saturation for the accelerated acquisition resulting in T1 underestimation for 19 of 21 slices across tissue species. The slices which do not demonstrate T1 saturation are anatomical slices 1 and 2, which are the first acquired slices within the odd and even slice groups. Although in the SSI scheme there is sufficient acquisition delay for the $+/-1$ nominal slice position (9.2 s), there is only a 0.84 s acquisition delay for the $+/-2$ nominal slice position. This short time delay does not allow recovery from the cross-talk effect of the inversion pulse with a slice thickness of 200% of the excitation pulse, causing T1 saturation in most of the slices. In the OSI scheme, the time delay between the $+/-1$ and $+/-2$ nominal slice positions was 4.2 and 5.9 s, respectively, which allows for recovery from the effect of the inversion pulse for abdominal tissues. As a result, no apparent T1 saturation is observed across slices in Figure 6C.

Figure 7 shows the result of linear regression analysis comparing estimated T1 values for liver, muscle, spleen, and kidney cortex between the accelerated single BH acquisitions (T1RC = 0.84 s) using SSI and OSI against the baseline (T1RC = 2.5 s) acquisition. For SSI (Figure 7A), the fit equation and goodness of fit were $y = 0.89x - 1.57$ and $R^2 = 0.89$, respectively. The slope is consistent with the observations of Figure 6, where T1 underestimation is observed across organs (and in this case across subjects) due to T1 saturation effects. The fit equation also demonstrates a relatively small bias, indicating that the degree of T1 underestimation is dependent on T1 value, and is more severe for longer T1 species. For OSI (Figure 7B), the fit equation and goodness of fit were $y = 0.99x + 23.2$ and $R^2 = 0.98$, respectively. The near-unity slope is consistent with Figure 6C, where no noticeable effects of T1 saturation were observed. This combined with the relatively small bias and high goodness of fit indicates that the accelerated technique combined with OSI results in T1 values which are highly concordant with the reference acquisition.

3.2.2 | PWF versus CNN

Figure 8 provides visual examples of the accelerated (T1RC = 0.84 s) 21-slice *single*-BHP acquisition in three representative slices. In the figure, T1 maps generated using the accelerated protocol with both PWF and the proposed CNN model are shown. For reference, T1 maps were acquired with the baseline 2.5 s T1RC protocol for the same prescribed anatomical volume, and similar anatomical slices are chosen for comparison. Note that within the kidneys (Figure 8A), there is improved sub-organ structure definition with CNN compared to PWF for T1RC = 0.84 s, improving boundary definition between the cortex and medullary regions. Within the spleen (Figure 8B), the PWF-estimated T1 map contains

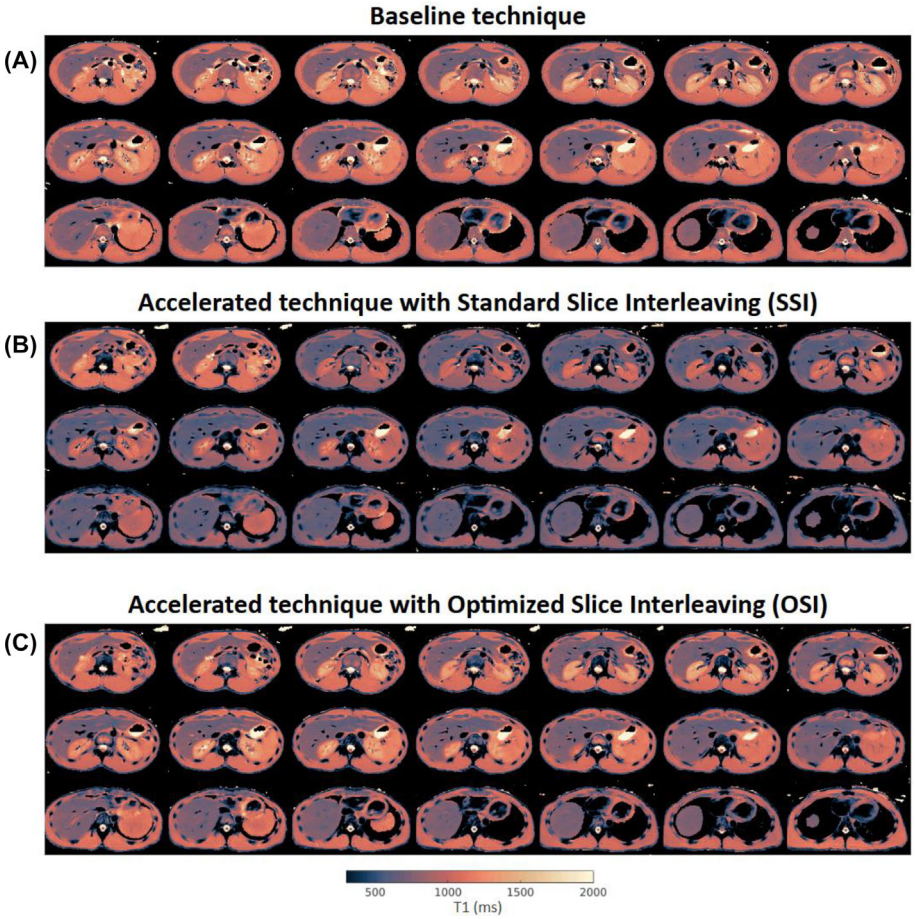

FIGURE 6 Comparison of 21-slice abdominal acquisitions using (A) the baseline three breath-hold technique (T1 recovery curve [T1RC] = 2.5 s and pixel-wise fitting [PWF]), and the single breath hold accelerated technique (T1RC = 0.84 s and convolutional neural network [CNN]) utilizing (B) standard slice interleaving (SSI) and (C) optimized slice interleaving (OSI). Acquired slices for all acquisitions are given in anatomical order.

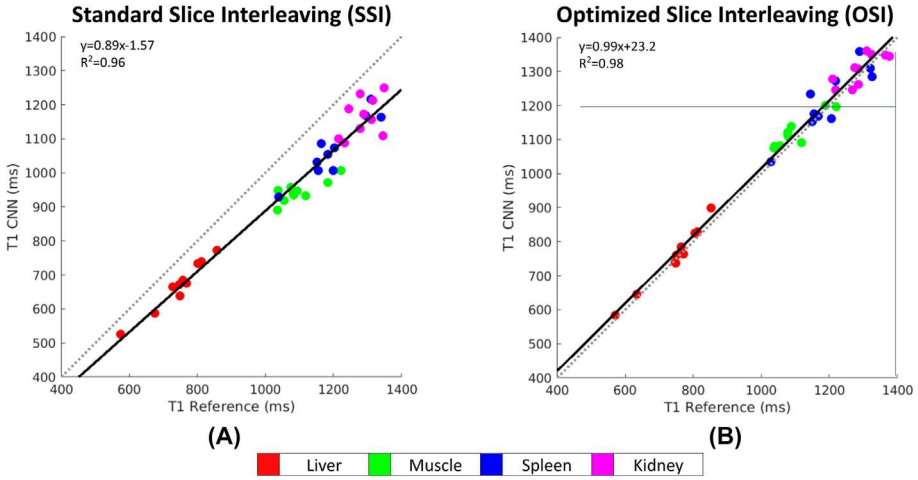

FIGURE 7 Linear regression analysis comparing convolutional neural network (CNN)-generated T1 estimates for 10 test subjects using the accelerated (T1 recovery curve [T1RC] = 0.84 s) 21-slice single breath hold acquisition with (A) standard slice interleaving (SSI) and (B) optimized slice interleaving (OSI) for regions-of-interest in liver, muscle, spleen, and kidney (cortex). The T1 reference is obtained using a baseline (T1RC = 2.5 s) 21-slice multi-breath hold period (BHP) acquisition.

significant noise in comparison to the CNN-generated map. An example of a liver lesion is shown in Figure 8C. While the PWF-generated T1 maps show significant degradation of the lesion internal contents and boundary, the CNN-generated T1 map is consistent with the reference.

Figure 9 compares T1 estimation between PWF and CNN in liver (L), muscle (M), spleen (S), and kidney cortex (K) for three test subjects when using the accelerated protocol (see Figure S1 for data corresponding to the remaining seven test subjects). The overall difference (across all 10 test subjects) in mean T1 for PWF (<2.2%) and CNN (<1.9%) remained low across subjects and tissue types. However, there was a clear difference in standard deviation in T1 across subjects. The standard deviations for CNN-generated T1 estimates (green) were [L,M,S,K] = [38, 42, 67, 102 ms], which are comparable to the reference acquisition (black) [L,M,S,K] = [41, 56, 63, 114 ms]. On the other hand, the T1 variability for PWF when using the accelerated sequence (red) was higher for all tissue ([L,M,S,K] = [47, 105, 144, 168 ms]).

3.2.3 | Repeatability

The results of repeatability experiments for the 10 test subjects are presented in Figure 10 for ROIs selected from liver, muscle, spleen, and kidney cortex. The fit equation and goodness of fit from linear regression analysis (Figure 10A) were $y = 0.98x + 6.34$ and $R^2 = 0.99$, respectively. The repeatability coefficient (RPC) and coefficient of variation (CV) from Bland–Altman analysis were 4.1% and 0.20%, respectively. These results collectively indicate strong agreement across imaging sessions when using the proposed accelerated technique.

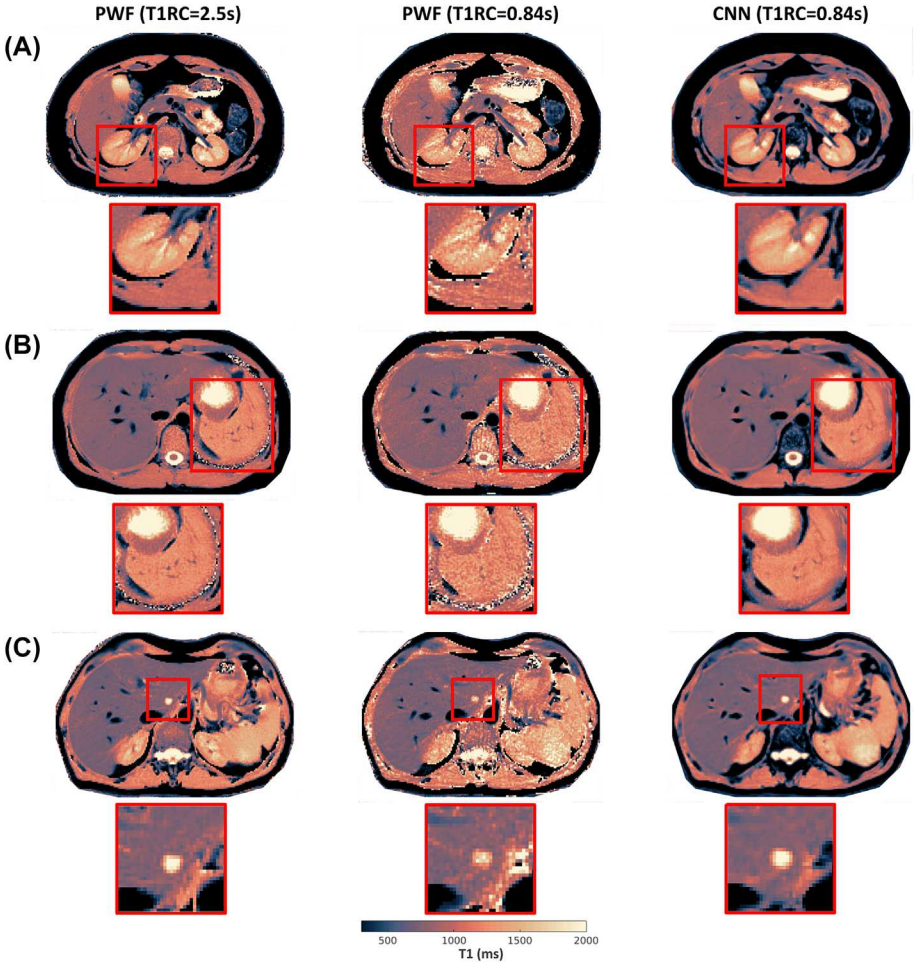

FIGURE 8 Representative T1 maps obtained prospectively with the accelerated 21-slice single breath hold (T1 recovery curve [T1RC] = 0.84 s) protocol with optimized slice interleaving (OSI). T1 maps from a reference scan with T1RC = 2.5 s and pixel-wise fitting (PWF) acquired within a separate breath hold period (BHP) are also shown. The nearest anatomical slice between the T1RC = 0.84 s and T1RC = 2.5 s acquisitions is selected for comparison. These examples show increased noise and structural degradation in (A) kidneys and (B) spleen, when the accelerated protocol with PWF is used. These artifacts are not seen in the convolutional neural network (CNN)-estimated T1 maps. For the liver lesion shown in (C), the accelerated protocol using PWF estimation is noisy, and the lesion boundary is not well defined. In contrast, the T1 values from the CNN estimate closely matches the reference, and lesion boundaries are well delineated.

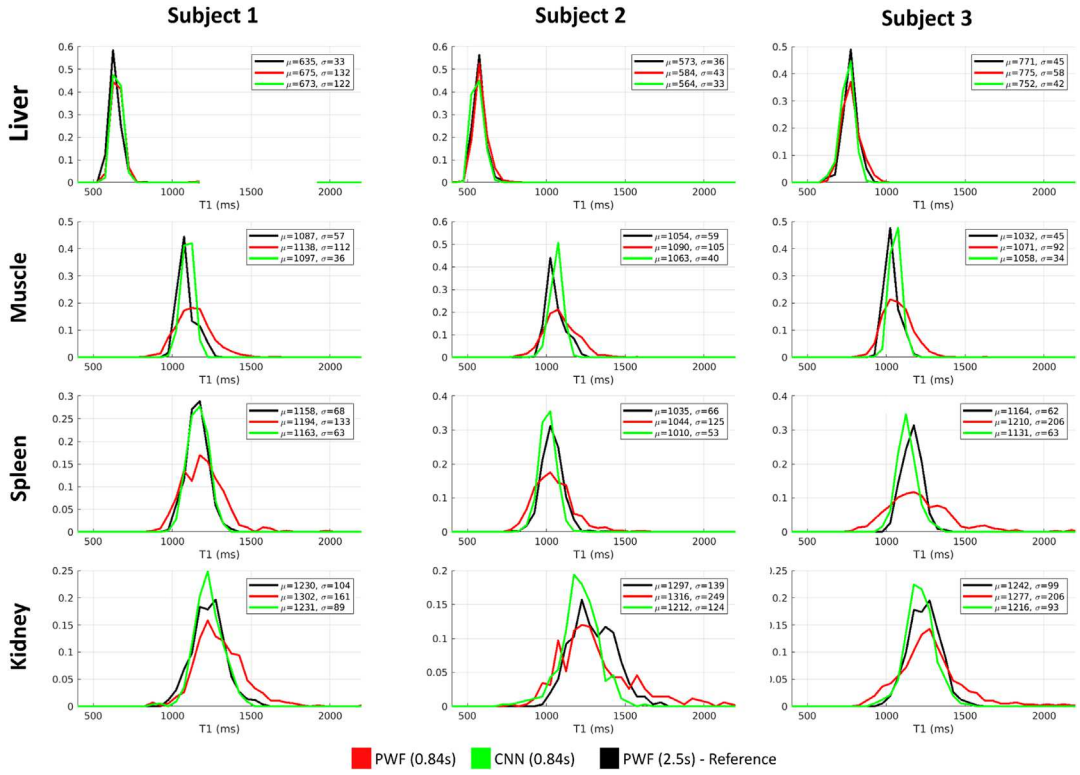

FIGURE 9 Distributions of T1 values obtained from the accelerated protocol (T1 recovery curve [T1RC] = 0.84 s with optimized slice interleaving [OSI]) with pixel-wise fitting (PWF) (red) and convolutional neural network (CNN) (green) T1 estimation. The reference distributions, obtained using the baseline protocol (T1RC = 2.5 s with standard slice interleaving [SSI]) with PWF, are shown in black The y-axis of each distribution represents relative frequency of T1 values for regions of interest stemming from liver, muscle, spleen, and kidney. Data for the remaining test subjects are provided in Figure S1.

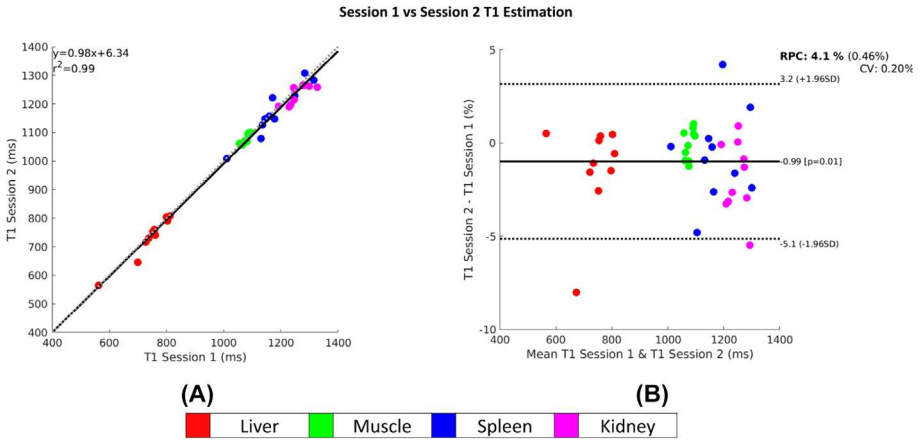

FIGURE 10 Repeatability analysis of the accelerated 21-slice single breath hold (T1 recovery curve [T1RC] = 0.84 s) protocol with optimized slice interleaving (OSI) using (A) correlation and (B) Bland–Altman plots. The plots were obtained by comparing T1 values in four organs between two imaging sessions for ten test subjects. CV, coefficient of variation; RPC, repeatability coefficient.

4 | DISCUSSION

This work introduced an accelerated T1 mapping method, based on a rapid T1RC ssIR radial Look-Locker technique coupled with an OSI scheme and DL T1 estimation, for efficient coverage of the abdomen within a single BHP. The impact of T1RC length on T1 estimation was assessed, and the advantages of using a DL approach for T1 estimation and optimized interleaving (implemented to minimize the dead time between the acquisition of neighboring slices) were presented. The accelerated T1 mapping protocol, which utilizes a 0.84 s T1RC, yields 21 slices within a single

20 s BHP allowing for full abdomen coverage. Because the acquisition is based on a radial k-space trajectory, and data for the IR curve are acquired in <1 s, the technique is motion robust. The technique is 10×–20× faster than Look-Locker T1 mapping protocols used in the clinic and 2× faster than a long-T1RC counterpart,[22,23] resulting in efficient anatomical coverage within a BHP.

In retrospective phantom and in vivo experiments, results based on a ROI analysis show an increase in T1 error with PWF compared to the proposed CNN approach when reducing T1RC.

When considering the mean T1 values for all pixels within the ROI, the bias is averaged out for both PWF and CNN even when T1RC is shortened down to 0.84 s. However, the precision of T1 estimation is negatively impacted by shortening of the T1RC when using the traditional PWF approach. Shortening of the T1RC results in a reduced number of TIs for T1 fitting and thus reduces the number of radial views available for joint iterative reconstruction. The latter is expected to have a negative impact on the quality of the reconstructed T1RC signal evolution, which, in turn, resulted in reduced fitting quality. Since the grouping of radial views per TI image is not fixed, it can be changed during reconstruction to produce more TI images for a given T1RC length. However, as shown in previous work, this will not likely result in improved T1 estimation performance.[23] By training the CNN using a reference long T1RC (2.5 s in vivo), we were able to avoid the shortcomings of the more traditional PWF and achieve T1 maps with less noise, thus maintaining precision for short-T1RC lengths.

The use of retrospective view truncation allowed efficient generation of training datasets over a range of input T1RC sampling lengths. This greatly reduced the number of subject acquisitions required to develop a dataset for model development and eliminated the need for image registration due to subject motion across breath holds between acquisitions. Comparison of retrospectively generated and prospectively acquired rapid T1RC datasets did not show a domain shift (see Section 3.2), and the CNNs trained on these simulated datasets performed well when applied to prospectively accelerated acquisition. These results indicate that the retrospective view truncation approach provides a good surrogate for prospectively accelerated sampling.

Because the ssIR pulse inverts a slice with twice the thickness of the excitation slice to achieve good inversion, neighboring slices experience a partial inversion. Reduction of the T1RC sampling window (with no inter-slice time delay) results in re-application of ssIR prior to complete relaxation of these neighboring tissue regions. For the proposed accelerated protocol, the time delay between the inversion of adjacent slices for SSI and OSI was sufficiently long for the recovery of abdominal tissues. However, the combination of a ssIR RF pulse with rapid T1RC sampling requires consideration of partial inversion beyond adjacent slices. For SSI, the minimum time delay between the inversion of slices within two slice positions of each other (i.e., consecutive odd or even slices) is only 0.84 s. Although the RF pulse is not 180° at these distances, the time delay is not sufficient to allow recovery from the extended effect of the inversion pulse. Meanwhile, for OSI, the minimum time delay between consecutive odd or even slices is 7× greater (5.9 s) than for SSI, which is sufficient for recovery of the extended effect of the inversion pulse. This efficient use of anatomy by OSI to spread out the ssIR over time allows acquisition of 21 slices within a 20 s BHP without T1 saturation.

While a 20 s BHP may be achievable for some subjects, this may not be the case for all. The OSI scheme presented here can also yield 17–18 slices with the T1RC of 0.84 s in an 18 s breath hold; to assure full abdominal coverage, a small inter-slice gap (1–2 mm) can be used. Shorter breath holds (e.g., 15 s) with full coverage would require a shorter T1RC. For breath holds in the order of 10–12 s, full abdominal coverage would require two breath holds. In this case, the slice SSI can be used with each slice group distributed over the full volume. Alternatively, recent studies in the brain have proposed neural network-based techniques to compensate for the effect of T1 saturation in Look-Locker acquisitions.[35] In future studies, it would be worthwhile to evaluate a similar approach for abdominal T1 mapping against the methodology presented here.

Although the proposed technique has been developed for breath hold T1 mapping, the framework may be extended to reduce the effect of motion in prospectively triggered free breathing acquisitions.[36] Due to the long sampling time typically required for T1 estimation, the later portion of the T1RC is susceptible to corruption due to subject motion. Reduction of the T1RC length reduces the risk of corruption, allowing for more robust T1 estimation.

The T1RC technique was demonstrated here using a single-echo Look-Locker technique. Recent studies have explored the use of multi-echo Look-Locker sequences for fat-water-separated T1 mapping.[24,25] In future work, we will extend our framework for this application by including more GREs per TR.[37]

The CNN model was developed using a limited 30-subject cohort of normal volunteers with fixed acquisition protocol. An extension of this work on a larger subject cohort, including those with pathologies, would allow for improvements in training by allowing use of more complex models and robust hyper-parameter optimization. The availability of datasets acquired with different acquisition protocols would allow for assessment of model sensitivity to different acquisition parameters (e.g., slice thickness, flip angle, and bandwidth), which could be incorporated to improve model robustness.

5 | CONCLUSION

An accelerated T1 mapping technique was proposed, which utilizes rapid sampling of the T1RC in single-shot slice-selective Look-Locker acquisitions to improve slice efficiency. A DL architecture was presented, which allows training of a CNN model to maintain T1 estimation performance

when given reduced quality T1RC signal stemming from accelerated acquisition. In vivo experiments demonstrated the utility of the proposed method. This approach provides a feasible alternative to current clinical protocols to allow wide abdominal coverage within a reasonable BHP.

CONFLICT OF INTEREST STATEMENT

Ute Goerke and Vibhas Deshpande are employees of Siemens Medical Solutions USA.

DATA AVAILABILITY STATEMENT

The source code used in this article is available upon reasonable request.

REFERENCES

1. Yoshimura N, Saito K, Saguchi T, et al. Distinguishing hepatic hemangiomas from metastatic tumors using T1 mapping on gadoxetic-acid-enhanced MRI. *Magn Reson Imaging*. 2013;31(1):23-27. doi:10.1016/j.mri.2012.06.026
2. Mio M, Fujiwara Y, Tani K, Toyofuku T, Maeda T, Inoue T. Quantitative evaluation of focal liver lesions with T1 mapping using a phase-sensitive inversion recovery sequence on gadoxetic acid-enhanced MRI. *Eur J Radiol*. 2021;8:100312.
3. Pavlides M, Banerjee R, Sellwood J, et al. Multiparametric magnetic resonance imaging predicts clinical outcomes in patients with chronic liver disease. *J Hepatol*. 2016;64(2):308-315. doi:10.1016/j.jhep.2015.10.009
4. Luetkens JA, Klein S, Traeber F, et al. Quantitative liver MRI including extracellular volume fraction for non-invasive quantification of liver fibrosis: a prospective proof-of-concept study. *Gut*. 2018;67(3):593-594. doi:10.1136/gutjnl-2017-314561
5. Hoad CL, Palaniyappan N, Kaye P, et al. A study of T_1 relaxation time as a measure of liver fibrosis and the influence of confounding histological factors. *NMR Biomed*. 2015;28(6):706-714. doi:10.1002/nbm.3299
6. Kim KA, Park MS, Kim IS, et al. Quantitative evaluation of liver cirrhosis using T1 relaxation time with 3 tesla MRI before and after oxygen inhalation. *J Magn Reson Imaging*. 2012;36(2):405-410. doi:10.1002/jmri.23620
7. Haimerl M, Verloh N, Zeman F, et al. Assessment of clinical signs of liver cirrhosis using T1 mapping on Gd-EOB-DTPA-enhanced 3T MRI. *PLoS ONE*. 2013;8(12):e85658. doi:10.1371/journal.pone.0085658
8. Tirkes T, Lin C, Fogel EL, Sherman SS, Wang Q, Sandrasegaran K. T_1 mapping for diagnosis of mild chronic pancreatitis. *J Magn Reson Imaging*. 2017;45(4):1171-1176. doi:10.1002/jmri.25428
9. Huang Y, Sadowski EA, Artz NS, et al. Measurement and comparison of T1 relaxation times in native and transplanted kidney cortex and medulla. *J Magn Reson Imaging*. 2011;33(5):1241-1247. doi:10.1002/jmri.22543
10. Messroghli DR, Radjenovic A, Kozerke S, Higgins DM, Sivananthan MU, Ridgway JP. Modified Look-Locker inversion recovery (MOLLI) for high-resolution T_1 mapping of the heart. *Magn Reson Med*. 2004;52(1):141-146. doi:10.1002/mrm.20110
11. Piechnik SK, Ferreira VM, Dall'Armellina E, et al. Shortened modified Look-Locker inversion recovery (ShMOLLI) for clinical myocardial T1-mapping at 1.5 and 3 T within a 9 heartbeat breathhold. *J Cardiovasc Magn Reson*. 2010;12(1):69. doi:10.1186/1532-429X-12-69
12. Cheng HLM, Wright GA. Rapid high-resolution T_1 mapping by variable flip angles: accurate and precise measurements in the presence of radiofrequency field inhomogeneity. *Magn Reson Med*. 2006;55(3):566-574. doi:10.1002/mrm.20791
13. Tirkes T, Zhao X, Lin C, et al. Evaluation of variable flip angle, MOLLI, SASHA, and IR-SNAPSHOT pulse sequences for T1 relaxometry and extracellular volume imaging of the pancreas and liver. *Magn Res Mater Phys Biol Med*. 2019;32(5):559-566. doi:10.1007/s10334-019-00762-2
14. Ma D, Gulani V, Seiberlich N, et al. Magnetic resonance fingerprinting. *Nature*. 2013;495(7440):187-192. doi:10.1038/nature11971
15. Chen Y, Jiang Y, Pahwa S, et al. MR fingerprinting for rapid quantitative abdominal imaging. *Radiology*. 2016;279(1):278-286. doi:10.1148/radiol.2016152037
16. Fujita S, Sano K, Cruz G, et al. MR fingerprinting for contrast agent-free and quantitative characterization of focal liver lesions. *Radiol Imaging Cancer*. 2023;5(6):e230036. doi:10.1148/rycan.230036
17. Buonincontri G, Sawiak SJ. MR fingerprinting with simultaneous B1 estimation. *Magn Reson Med*. 2016;76(4):1127-1135. doi:10.1002/mrm.26009
18. Ma D, Coppo S, Chen Y, et al. Slice profile and B_1 corrections in 2D magnetic resonance fingerprinting. *Magn Reson Med*. 2017;78(5):1781-1789. doi:10.1002/mrm.26580
19. Chen Y, Lee GR, Aandal G, et al. Rapid volumetric T1 mapping of the abdomen using three-dimensional through-time spiral GRAPPA. *Magn Reson Med*. 2016;75(4):1457-1465. doi:10.1002/mrm.25693
20. Griswold MA, Jakob PM, Heidemann RM, et al. Generalized autocalibrating partially parallel acquisitions (GRAPPA). *Magn Reson Med*. 2002;47(6):1202-1210.
21. Feng L, Liu F, Soultanidis G, et al. Magnetization-prepared GRASP MRI for rapid 3D T1 mapping and fat/water-separated T1 mapping. *Magn Reson Med*. 2021;86(1):97-114. doi:10.1002/mrm.28679
22. Wang X, Rosenzweig S, Scholand N, Holme HCM, Uecker M. Model-based reconstruction for simultaneous multi-slice T1 mapping using single-shot inversion-recovery radial FLASH. *Magn Reson Med*. 2021;85(3):1258-1271. doi:10.1002/mrm.28497
23. Li Z, Bilgin A, Johnson K, et al. Rapid high-resolution T_1 mapping using a highly accelerated radial steady-state free-precession technique. *J Magn Reson Imaging*. 2019;49(1):239-252. doi:10.1002/jmri.26170
24. Li Z, Mathew M, Syed AB, et al. Rapid fat-water separated T_1 mapping using a single-shot radial inversion-recovery spoiled gradient recalled pulse sequence. *NMR Biomed*. 2022;35(12):e4803. doi:10.1002/nbm.4803
25. Moquillaza EH, Weiss K, Stelter J, et al. Accelerated liver water T_1 mapping using single-shot continuous inversion-recovery spiral imaging. *NMR Biomed*. 2024;37(5):e5097. doi:10.1002/nbm.5097
26. Goerke U, Ahanonu E, Keerthivasan M, Bilgin A, Deshpande V, Altbach M. Inversion recovery Look-Locker T1-mapping for abdominal imaging: how many slices can one fit in a single breath-hold? In: *Proc Intl Soc Mag Reson Med*. 2022;30:107.
27. Zhao B, Lu W, Hitchens KT, Lam F, Ho C, Liang ZP. Accelerated MR parameter mapping with low-rank and sparsity constraints. *Magn Reson Med*. 2015;74(2):489-498. doi:10.1002/mrm.25421

28. Saucedo S, Lefkimmiatis S, Rangwala N, Sung K. Improved computational efficiency of locally low rank MRI reconstruction using iterative random patch adjustments. *IEEE Tran Med Imaging*. 2017;36(6):1209-1220. doi:10.1109/TMI.2017.2659742
29. Blumenthal M, Holme C, Roeloffs V, et al. BART: computational magnetic resonance imaging. 10.5281/zenodo.592960.
30. Knoll F, Schwarzl A, Diwoky C, Sodickson DK. gpuNUFFT—an open source GPU library for 3D regridding with direct Matlab interface. In: *Proc Intl Soc Mag Reson Med*. 2014;22:4297.
31. Barral JK, Gudmundson E, Stikov N, Etezadi-Amoli M, Stoica P, Nishimura DG. A robust methodology for in vivo T_1 mapping. *Magn Reson Med*. 2010; 64(4):1057-1067. doi:10.1002/mrm.22497
32. Abadi M, Agarwal A, Barham P, et al. TensorFlow: large-scale machine learning on heterogeneous distributed systems. 2015. 10.48550/arXiv.1603.04467.
33. He K, Zhang X, Ren S, Sun J. Deep residual learning for image recognition. In: *IEEE Computer Vision and Pattern Recognition (CVPR)*; 2016;770-778.
34. Kingma DP, Ba J. Adam: a method for stochastic optimization. In: *International Conference on Learning Representations (ICLR)*; 2015; Poster.
35. Pei H, Xia D, Xu X, et al. Rapid 3D T_1 mapping using deep learning-assisted Look-Locker inversion recovery MRI. *Magn Reson Med*. 2023;90(2):569-582. doi:10.1002/mrm.29672
36. Ahanonu E, Johnson K, Goerke U, et al. T1 mapping of the entire abdomen using a time efficient free breathing neural network radial Look Locker approach. In: *Proc Intl Soc Mag Reson Med*. 2023;31:664.
37. Ahanonu E, Goerke U, Toner B, et al. Hybrid multi-echo radial Look-Locker (hME-rLL) acquisition for joint estimation of water-T1, PDFF, and R2*. In: *Proc Intl Soc Mag Reson Med*. 2024;32:146.

SUPPORTING INFORMATION

Additional supporting information can be found online in the Supporting Information section at the end of this article.

How to cite this article: Ahanonu E, Goerke U, Johnson K, et al. Accelerated 2D radial Look-Locker T1 mapping using a deep learning-based rapid inversion recovery sampling technique. *NMR in Biomedicine*. 2024;37(12):e5266. doi:10.1002/nbm.5266